Research Square

Preprints are preliminary reports that have not undergone peer review.
They should not be considered conclusive, used to inform clinical practice,
or referenced by the media as validated information.

A Wide-Voltage-Range Input High-Power-Density Three-Phase Grid-Frequency Isolated Inverter

Yong Tang
Nanchang Institute of Science and Technology
Huiying Tang
huiyingtang2024@126.com
School of Mechanical and Electrical Engineering
Bo Wang
Nanchang Institute of Science and Technology

Research Article

Keywords: wide voltage input, multiplex technology, carrier phase shift, 3D wound core, double-Fourier analysis, power density

Posted Date: March 13th, 2026

DOI: https://doi.org/10.21203/rs.3.rs-8947226/v1

License: This work is licensed under a Creative Commons Attribution 4.0 International License.
Read Full License

Additional Declarations: No competing interests reported.

A Wide-Voltage-Range Input High-Power-Density Three-Phase Grid-Frequency Isolated Inverter

Yong Tang[1], Huiying Tang[2], Bo Wang[1]
[1]School of Information and Artificial Intelligence, Nanchang Institute of Science and Technology, Nanchang, 330108, China
[2]School of Mechanical and Electrical Engineering, Wuhan Donghu University, Wuhan, 430212, China

Corresponding author: Huiying Tang, China (e-mail: huiyingtang2024@126.com).

ABSTRACT As shipboard distribution systems keep advancing toward miniaturization, integration, and high efficiency, energy storage components have become an integral part of the distribution system. Three-phase inverters are confronted with challenges including a broad DC input voltage range, stringent AC power quality standards, and the demand for high power density. This study presents a hybrid three-phase dual-stage inverter topology that markedly enhances the equivalent switching frequency via multiphase technology, realizing a five-level phase voltage with a fourfold frequency gain and thus lowering the requirement for LC filters. The adoption of a carrier phase-shifting (CPS) modulation scheme effectively suppresses the output common-mode (CM) voltage, thus significantly reducing the design requirements for EMI filters. Through the application of integrated transformer magnetic circuit technology and a three-dimensional (3D) coiled core structure, the overall size and weight of isolation transformers and filter inductors have been significantly reduced. Moreover, the series connection of the transformer's secondary windings enhances the peak amplitude of the AC output voltage while further improving the utilization efficiency of the DC voltage. Through these comprehensive measures, the designed distribution system inverter exhibits the advantages of high system efficiency, strong reliability, cost-effectiveness, compact size, and light weight, making it particularly suitable for high-power applications requiring isolated wide-range DC voltage inputs.

INDEX TERMS wide voltage input; multiplex technology; carrier phase shift; 3D wound core; double-Fourier analysis; power density

I. Introduction

The integrated power system of ships incorporates power generation systems, power conversion and distribution systems, propulsion systems, and other related equipment to realize unified electrical dispatch and centralized power management. It is the development trend of marine power systems [1]. As research progresses, distribution systems are evolving toward miniaturization, integration, and high efficiency. Energy storage has become an essential component of power generation systems to ensure electrical energy quality. However, connecting energy storage batteries to the DC power grid introduces practical challenges for three-phase isolated inverters used in marine applications, which are featured by a DC voltage range (400-700 V), strict AC power quality requirements, and the demand for higher power density [2].

To achieve electrical isolation between input and output, the most conventional solution is to directly incorporate grid-frequency transformers between filters and loads. Grid-frequency isolated inverters boast mature technology and exhibit reliable electrical performance, delivering relatively high conversion efficiency and gaining widespread application. Nevertheless, they have inherent limitations such as low operating frequency, bulky transformers, heavy weight, high manufacturing costs, low power density, and suboptimal dynamic performance[3]. In an effort to reduce inverter size and weight while increasing system power density, many studies proposed the use of high-frequency transformers to replace grid-frequency transformers for isolation [4-8]. Two common approaches are the two-stage and single-stage high-frequency isolated inverter solutions. Among these, the two-stage high-frequency isolated inverter offers the advantage of mature technology at each conversion stage [9-12], allowing independent control of front and rear stages, thereby enhancing flexibility. However, it suffers from the drawback of having multiple energy transfer stages, which reduces system conversion efficiency. By contrast, the high-frequency single-stage

isolated inverter features fewer conversion stages and components, along with lower costs and higher operational efficiency [13-18]. Nevertheless, single-stage inverters of this type encounter certain issues: firstly, the switching devices are typically hard-switched, leading to high switching losses, and secondly, output filters with filtering inductors are bulky and heavy. More critically, during dead time or sudden power loss in the control system, the filtering inductor current lacks a return path, which can result in high-voltage breakdown of power switching devices, compromising system safety and reliability.

In marine distribution systems, to increase the power density of three-phase inverter sources [19-24], high-frequency isolation topologies can be adopted. However, the wide range of DC voltage fluctuations caused by energy storage integration makes it challenging to design the soft-switching operating points of DC-DC converters. This results in high switching losses and low converter efficiency, as well as reliability issues [25-30]. Considering factors such as reliability, efficiency, heat dissipation, and cost, grid-frequency isolation topologies are more suitable for practical engineering applications. However, compared to high-frequency isolation topologies, addressing the issue of increased power density remains an urgent concern.

This study presents a dual-stage grid-frequency isolated three-phase inverter topology, which integrates multiphase technology to boost the equivalent switching frequency while minimizing the specifications of output LC (inductor-capacitor) filters. Furthermore, a phase-shifted carrier modulation approach is utilized to mitigate the output CM voltage, thereby reducing the requirements for electromagnetic interference (EMI) filters. To achieve miniaturization and lightweight design of isolation transformers and filter inductors, magnetic integration technology, together with a 3D core configuration, is adopted for system optimization. Additionally, connecting the transformer's secondary windings in series enhances the AC output voltage amplitude and increases the utilization rate of the input DC voltage. Consequently, the proposed topology is particularly well-suited for high-power applications demanding isolated wide-range DC voltage inputs, featuring prominent advantages including high system efficiency, reliable operation, cost-effectiveness, and compact footprint.

II. Research on multiphase technology in novel topology

A. Main circuit of novel three-phase dual-stage topology

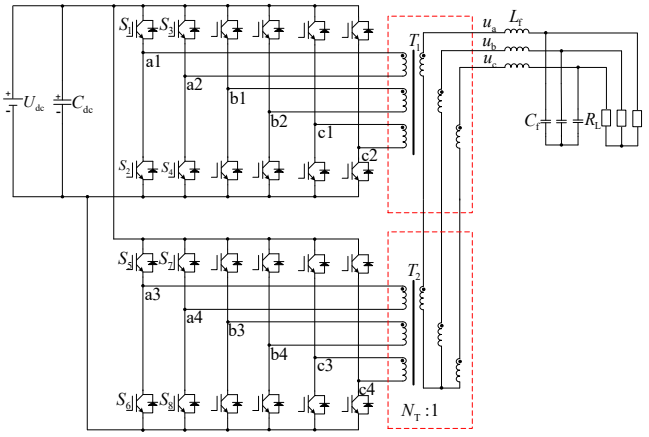


FIGURE 1. **Three-phase dual full-bridge integrated inverter**

Fig. 1 depicts the novel three-phase dual-stage inverter topology proposed in this work. This configuration adopts two sets of three-phase full-bridge inverters, which are serially connected via two Y/Y-connected transformers on their secondary side. In the topology, each H-bridge is operated with unipolar pulse-width modulation (PWM), meanwhile, a phase-shifted carrier modulation approach is adopted between the two H-bridges corresponding to each phase. The integration of CPS modulation into the dual H-bridge cascaded topology remarkably boosts the effective switching frequency. The main circuit is composed primarily of input support capacitors, three-phase full-bridge power units, transformers (T_1, T_2), and LC filters (L_f, C_f), with L_f corresponding to the transformer leakage inductance.

B. Novel topology modulation strategy

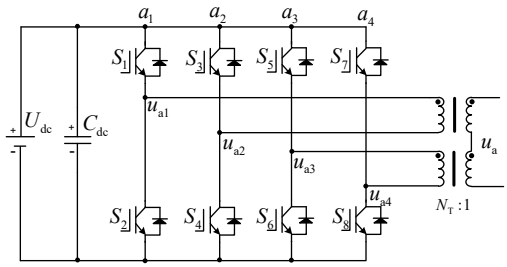


FIGURE 2. **Dual-group CPS modulation H-bridge equivalent circuits**

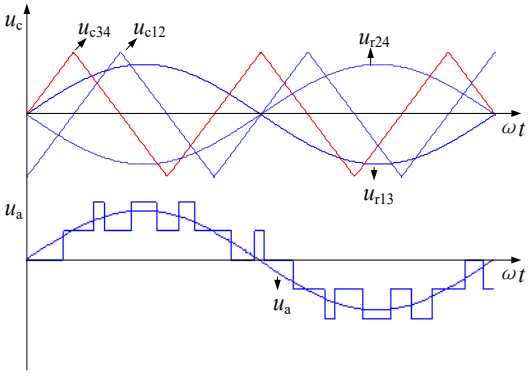


FIGURE 3. Five-level CPS modulation equivalent diagram

Fig. 2 presents the circuit configuration of two H-bridges serially interconnected via the secondary windings of a transformer. In this diagram, a_1, a_2, a_3, and a_4 denote the four half-bridge modules arranged from left to right, where a_1 and a_2 form the first H-bridge unit, and a_3 and a4 compose the second unit. The output voltages of these two units are defined as u_{a1a2} and u_{a3a4}, respectively; with these voltages applied in series and superimposed on the transformer secondary side, the integrated output voltage is defined as u_a. Unipolar PWM is adopted for each individual H-bridge, whereas a CPS modulation scheme is adopted between the two H-bridge modules, as illustrated in Fig. 3. Specifically, u_{c12} serves as the carrier signal for the first H-bridge's arms (a_1 and a_2), and u_{c34} acts as the carrier signal for the second H-bridge's arms (a_3 and a_4), with a 90° phase shift existing between u_{c12} and u_{c34}. Meanwhile, u_{r13} represents the modulation wave corresponding to arms a_1 and a_3, and u_{r24} represents that for arms a_2 and a_4, featuring a 180° phase shift between u_{r13} and u_{r24}. As observed from Fig. 3, the proposed equivalent modulation strategy enables the output phase voltage to achieve a fourfold frequency multiplication and a five-level output characteristic, thereby offering a more intuitive and clear physical interpretation.

C. Harmonic analysis of output phase voltage

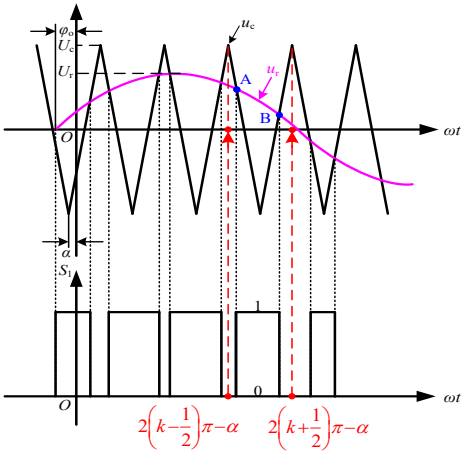


FIGURE 4. Working Principle of a Half-Bridge Inverter

Fig. 4 illustrates the control principle of a half-bridge inverter based on sinusoidal pulse width modulation (SPWM). For the sake of analytical simplicity, the triangular carrier wave is decomposed into two linear segments with slopes of $+2U_c/\pi$ and $-2U_c/\pi$, respectively. Where U_c denotes the amplitude of the triangular wave, and T_c represents its switching period. Accordingly, the mathematical expression of the triangular carrier wave is derived as follows:

$$\begin{cases} -\left[\omega_c t+\alpha-2k\pi\right]\dfrac{2U_c}{\pi}-U_c & 2\left(k-\dfrac{1}{2}\right)\pi-\alpha\le\omega_c t\le 2k\pi-\alpha \\ \left(\omega_c t+\alpha-2k\pi\right)\dfrac{2U_c}{\pi}-U_c & 2k\pi-\alpha\le\omega_c t\le 2\left(k+\dfrac{1}{2}\right)\pi-\alpha \end{cases} \tag{1}$$

where ω_c denotes the angular frequency of the triangular carrier wave; α represents the initial phase angle of the triangular carrier wave; and k takes integer values of 0, 1, 2, ...

The mathematical expression corresponding to the sinusoidal modulation wave is presented as follows:

$$u_r = U_r\cdot\sin\left(\omega_o t+\varphi_o\right) \tag{2}$$

Let the modulation ratio $M = U_r/U_c \le 1$, with U_c being held constant.

The double Fourier series corresponding to the two-level SPWM switching function sa1 (x, y) is derived as follows:

$$\begin{aligned} s_{a1} &= \frac{1}{2}+\frac{M}{2}\sin(\omega_o t+\varphi_o) \\ &+\frac{2}{\pi}\sum_{n=1,3,5\cdots}^{+\infty}\frac{1}{m}J_0\left(\frac{mM\pi}{2}\right)e^{-jm\alpha}\sin\frac{m\pi}{2}\cos\left(m\omega_c t\right) \\ &+\frac{2}{\pi}\sum_{m=1,2,3\cdots}^{+\infty}\sum_{n=\pm1,\pm2\cdots}^{\pm\infty}\frac{1}{m}J_n\left(\frac{mM\pi}{2}\right)e^{-jm\alpha}\sin\left(\frac{m+n}{2}\pi\right) \\ &\times\cos\left[m\omega_c t+n\left(\omega_o t+\varphi_o\right)-\frac{n\pi}{2}\right] \end{aligned} \tag{3}$$

Similarly, the switch functions s_{a2}, s_{a2}, and s_{a4} for arms a_2, a_3, and a_4 can be derived, respectively. As the turns ratio for transformers T_1 and T_2 is defined as N_T:1, the voltage on the transformer secondary side of each transformer can be formulated with reference to the schematic shown in Fig. 2.

$$\begin{aligned} u_a &= (u_{a1a2}+u_{a3a4})/N_T = U_{dc}\left[(s_{a1}-s_{a2})+(s_{a3}-s_{a4})\right]/N_T \\ &= \frac{2MU_{dc}}{N_T}\sin(\omega_o t+\varphi_o) \\ &+\frac{2U_{dc}}{\pi N_T}\sum_{m=1,2\cdots}^{+\infty}\sum_{n=-\infty}^{+\infty}\frac{1}{m}J_{2n-1}(2mM\pi)\cos\left[(2m+n-1)\pi\right]\sin\left[4m\omega_c t+(2n-1)(\omega_o t+\varphi_o)\right] \end{aligned} \tag{4}$$

Equation (4) describes the output voltage ua of phase A for the proposed three-phase dual-stage inverter under five-level PWM modulation based on CPS method, which is illustrated in Fig. 3. In this expression, the first term corresponds to the fundamental component of u_a, with an amplitude of $2MU_{dc}/N_T$. In contrast to conventional three-phase inverters, the amplitude value of the output AC voltage's fundamental component is doubled, which is perfectly consistent with the multiplicity characteristic. The second term denotes the harmonic component of u_a; these harmonics are concentrated in the sidebands adjacent to $4m\omega_c$, thereby realizing a fourfold frequency regulation effect.

III. Research on CPS modulation in the novel topology

A. Derivation of CM Voltage Expression

According to the standard definition for CM voltage in three-phase inverter systems, the magnitude of the CM voltage corresponding to the newly developed three-phase dual-stage topology presented in Fig. 1 is defined via Equation (5).

$$u_{cm} = \frac{1}{12}\sum_{i=1}^{4}\left(u_{ai} + u_{bi} + u_{ci}\right) \tag{5}$$

By applying the same logic, double Fourier series expressions associated with the switching functions of each bridge arm can be systematically derived, thereby yielding the final formulation of the CM voltage for the hybrid three-phase dual-stage topology, as specified in Equation (6).

$$\begin{aligned} u_{cm} &= \frac{1}{12}\sum_{i=1}^{4}\left(u_{ai} + u_{bi} + u_{ci}\right) \\ &= \frac{\sqrt{2}U_{dc}}{\pi}\sum_{m=1,2\cdots}^{+\infty}\frac{1}{2m-1}J_0\left(\frac{2m-1}{2}M\pi\right)\sin\frac{2m-1}{2}\pi\cos\left[(2m-1)\omega_c t\right] \\ &+ \frac{\sqrt{2}U_{dc}}{\pi}\sum_{m=1,2\cdots}^{+\infty}\sum_{n=-\infty}^{+\infty}\frac{1}{2m-1}J_{6n}\left(\frac{2m-1}{2}M\pi\right)\cos\left(m+3n-1\right)\pi\sin\left[(2m-1)\omega_c t+6n\left(\omega_o t+\varphi_o\right)\right] \end{aligned} \tag{6}$$

Equation (6) establishes the explicit expression corresponding to the CM voltage exhibited by the integrated three-phase dual-stage inverter topology.

B. Mitigating CM voltage via CPS modulation

Conventional sinusoidal pulse width modulation (SPWM) control schemes inherently induce CM voltages, with the most severe condition arising when all upper (or lower) bridge arms conduct synchronously, thus leading to a zero-state operation. To alleviate the adverse effects of such zero states, the CPS modulation strategy can be adopted to mitigate the CM voltage of the inverter. In the following chapters, this research explores the impacts of carrier phase-shift angles on the magnitude of CM voltage.

According to the volt-second balance principle, tuning the carrier signal phase does not affect the fundamental voltage amplitude at the inverter output. With reference to the CM voltage expression in Equation (8), and using the Phase A carrier phase as the benchmark, we have two degrees of freedom for interphase carrier phase shifting (namely, the phase-shift angles corresponding to the Phase B and Phase C carriers). Through scanning simulation of the Phase B and Phase C carrier angles with a 10° step size, we can obtain the CM voltage amplitude of the three-phase inverter under different carrier phase configurations, as shown in Fig. 5. The results indicate that both the amplitude and RMS value of the CM voltage reach their minimums when the carrier phase combinations of Phases A, B, and C are configured as (0°, -120°, 120°) or (0°, 120°, -120°).

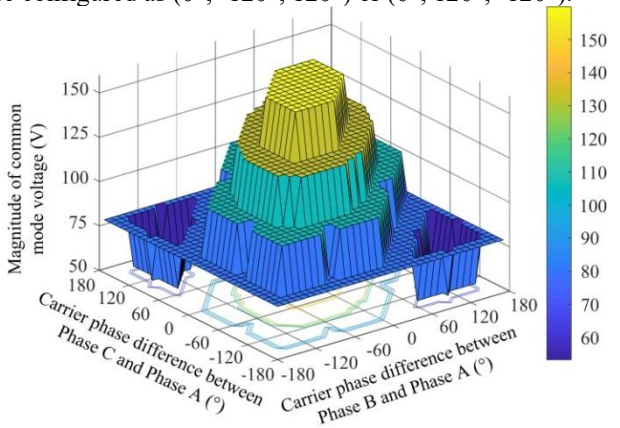
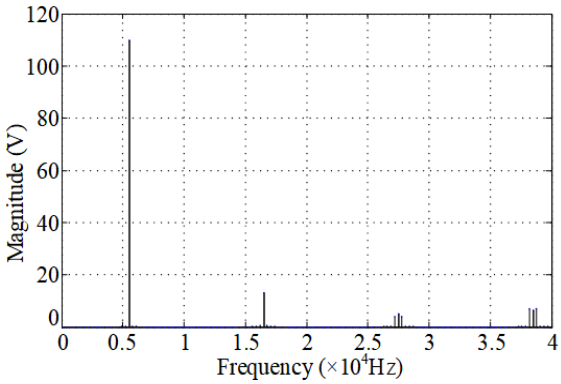


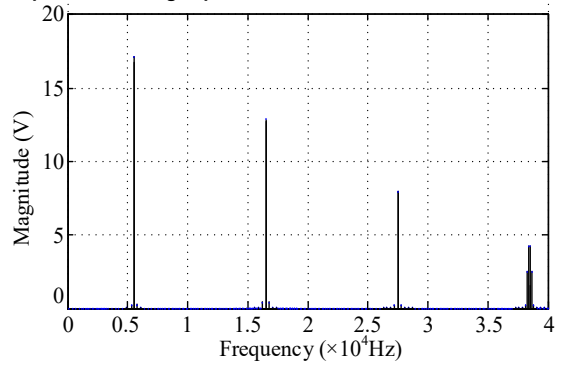
FIGURE 5. Impact of CPS angles on inverter output CM voltage

Where A-phase, B-phase, and C-phase triangular carrier phase angles are defined as 0, -2π/3, and 2π/3, respectively. The expression for the CM voltage is given by Equation (7).

$$\begin{aligned} u_{cm} &= \frac{1}{12}\sum_{i=1}^{4}\left(u_{ai} + u_{bi} + u_{ci}\right) \\ &= \frac{\sqrt{2}U_{dc}}{\pi}\sum_{m=1,2\cdots}^{+\infty}\frac{1}{6m-3}J_0\left(\frac{6m-3}{2}M\pi\right)\sin\frac{6m-3}{2}\pi\cos\left[(6m-3)\omega_c t\right] \\ &+ \frac{\sqrt{2}U_{dc}}{\pi}\sum_{m=1,2\cdots}^{+\infty}\sum_{n=-\infty}^{+\infty}\frac{1}{6m-3}J_{6n}\left(\frac{6m-3}{2}M\pi\right)\cos\left(3m+3n-2\right)\pi\sin\left[(6m-3)\omega_c t+6n\left(\omega_o t+\varphi_o\right)\right] \\ &+ \frac{U_{dc}}{\pi}\sum_{m=1,2\cdots}^{+\infty}\sum_{n=-\infty}^{+\infty}\frac{1}{2m-1}J_{6n+2}\left(\frac{2m-1}{2}M\pi\right)\cos\left(m+3n\right)\pi\sin\left[(2m-1)\omega_c t+(6n+2)\left(\omega_o t+\varphi_o\right)+\pi/4\right] \\ &+ \frac{U_{dc}}{\pi}\sum_{m=1,2\cdots}^{+\infty}\sum_{n=-\infty}^{+\infty}\frac{1}{2m-1}J_{6n+4}\left(\frac{2m-1}{2}M\pi\right)\cos\left(m+3n+1\right)\pi\sin\left[(2m-1)\omega_c t+(6n+4)\left(\omega_o t+\varphi_o\right)-\pi/4\right] \end{aligned} \tag{7}$$



(a) Computed CM voltage spectrum under non-CPS conditions



(b) Computed CM voltage spectrum under CPS conditions

FIGURE 6. Calculated results of inverter output CM voltage spectrum

Equation (7) delineates the common-mode (CM) voltage expression corresponding to the integrated three-phase dual-stage inverter that adopts the CPS modulation strategy. The calculated frequency spectrum of the CM voltage is depicted in Fig. 6. The adoption of the CPS modulation strategy can effectively suppress the amplitude of the CM voltage, which in turn contributes to a substantial reduction in the volume and weight of the output EMI filter and a simultaneous improvement in the power density of the entire device.

IV. Research on magnetic integration in the novel topology

Magnetic integration adopted in this research covers three key aspects: 1) integration of magnetic core circuits; 2) replacement of the conventional flat laminated core structure

with a 3D wound core structure; 3) integration of filter inductors into the leakage inductance of the isolation-type transformer.

The design methodology for magnetic core circuit integration is depicted in Fig. 7, which involves iterative design processes for six single-winding transformers, three three-winding transformers, and two six-winding transformers. The proposed design scheme helps cut down the size and weight of the transformers, and further boosts the overall power density. In comparison with the final configuration equipped with six single-phase windings, the two six-winding transformers achieve a volume reduction of approximately 20% and a weight reduction of around 12%.

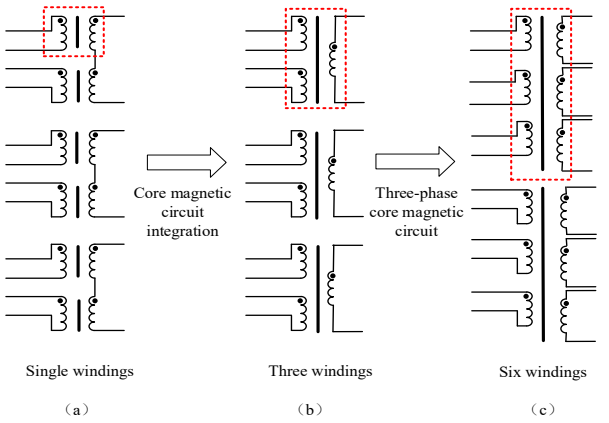
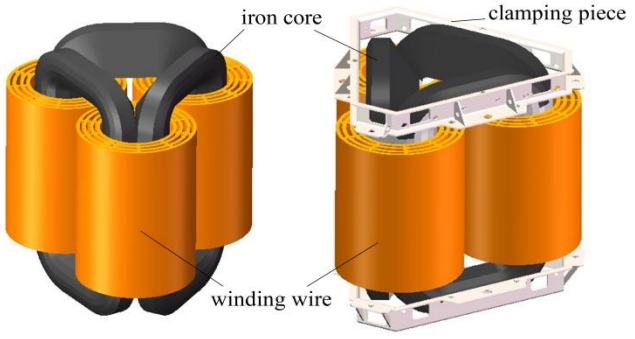


FIGURE 7. Design of Magnetic Integration for Combined Isolation Transformer Cores

The 3D wound core transformers possess inherent advantages including magnetic symmetry and lightweight construction. These transformers are capable of improving output harmonic performance while reducing overall volume and weight. In comparison with conventional three-phase flat laminated core transformers, the proposed transformer achieves a volume reduction of approximately 10% and a weight decrease of around 15%. The iron core structure adopted in this research is illustrated in Fig. 8.



(a) Core and winding **(b) Assembly draft**

FIGURE 8. 3D wound core transformer

The topology presented in this research employs multiphase technology to boost the effective switching frequency. Theoretical calculations show that the demanded output filter inductance is around 60μH. Therefore, it is feasible to replace the independent output filter inductor with the properly optimized leakage inductance of the transformer, which in turn improves the system's power density. During the transformer design and analysis stage, the frequency-related properties of winding impedance are incorporated into the design. The effectiveness of the proposed design is verified by comparing the time-domain simulation results of the transformer's frequency-dependent leakage inductance magnetic circuit model (as shown in Fig. 9) with the calculation outcomes derived from the two-dimensional equivalent model of the finite element method (FEM), as well as the experimental measurement data.

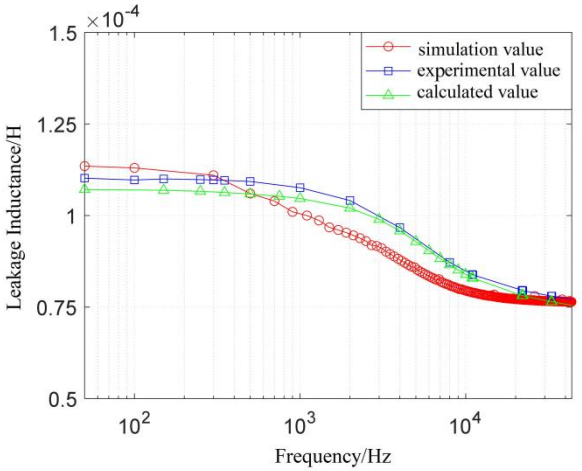


FIGURE 9. A comparative analysis of leakage inductance: experimental measurements vs. FEM calculations and time-domain simulations

As can be observed from Fig. 9, the experimental values show a close correlation with the calculated and simulated results. For the 3D wound core transformer, its leakage inductance maintains a value of approximately 110 μH or higher at frequencies below 1 kHz, and stays at around 75 μH or more within the frequency range of 1 kHz to 40 kHz. This performance fully satisfies the output filter inductance requirements of the three-phase dual-stage inverter. Therefore, the transformer's leakage inductance can be directly employed to substitute the dedicated output filter inductor, which further contributes to the reduction of the device's overall volume and weight.

V. Experimental validation

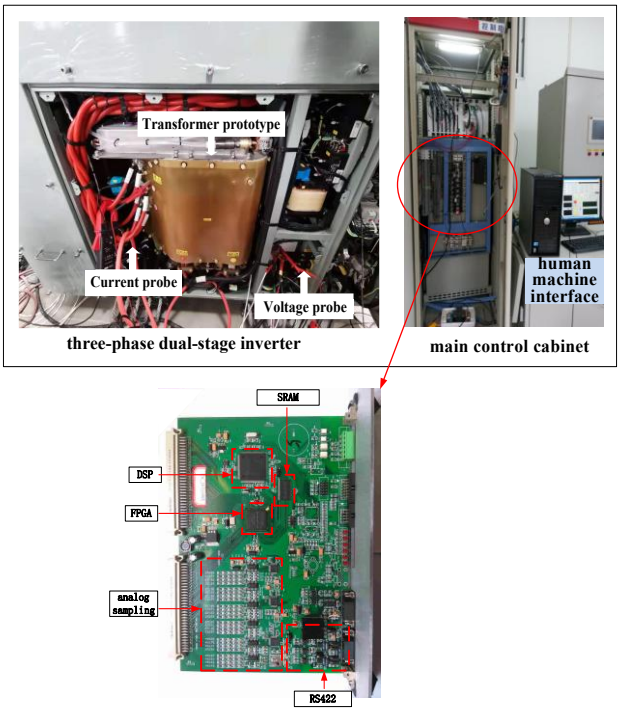


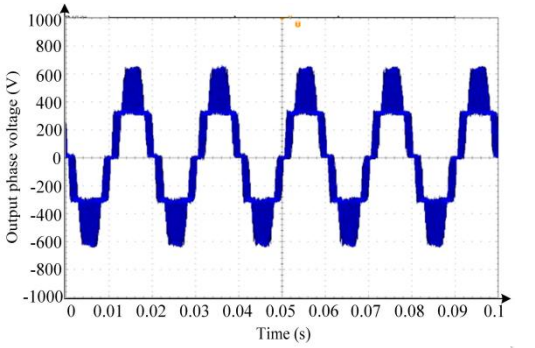
FIGURE 10. Experimental platform

For the purpose of verifying the accuracy and validity of the proposed novel three-phase dual-stage inverter topology, a prototype was built to conduct experimental validation. The core parameters of the prototype are tabulated in Table 1, while the experimental test bench is presented in Fig. 10. The acquired experimental waveforms are illustrated in Figs. 11 to 15.

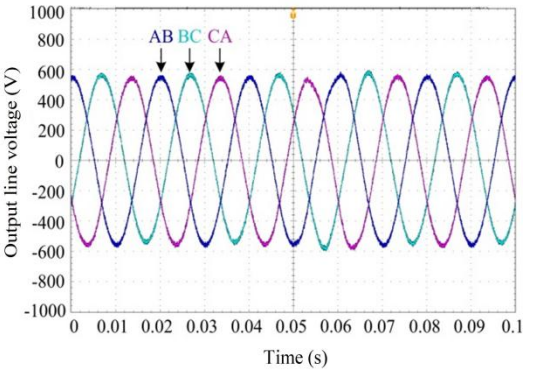
TAB.1 PARAMETERS OF THE PROTOTYPE INVERTER

Parameter	Value
DC input voltage U_{dc}	400~700V
output line voltage U_{line}	390V
output fundamental frequency f_o	50Hz
output active power P_o	130kW
power factor cosφ	0.8
ratio of transformer N_T	1
switching frequency f_{sw}	5.5kHz

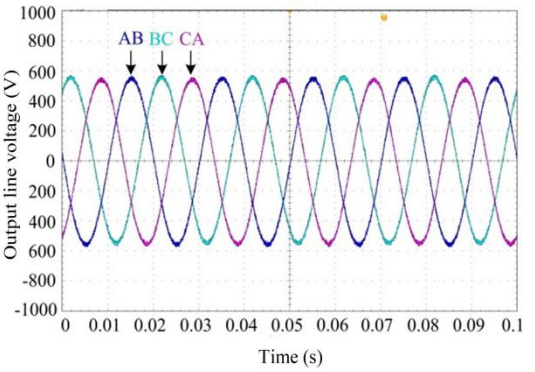
As shown in Fig.11 and Fig.12, the proposed novel topology realizes a five-level characteristic of the phase voltage, and its equivalent switching frequency reaches as high as 22 kHz. Within the DC voltage fluctuation range of 400 V to 700 V, the output AC voltage finishes adjustment within half a mains frequency cycle. Under rated inductive load and 35% nonlinear load operating conditions, the total harmonic distortion (THD) values of the phase voltage u_a are 1.71% and 3.85%, respectively.



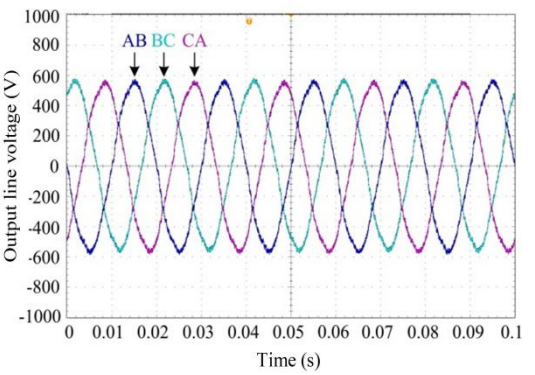
(a) A-phase voltage of transformer secondary side A-phase voltage



(b) Line voltage with DC input 400V-700V step



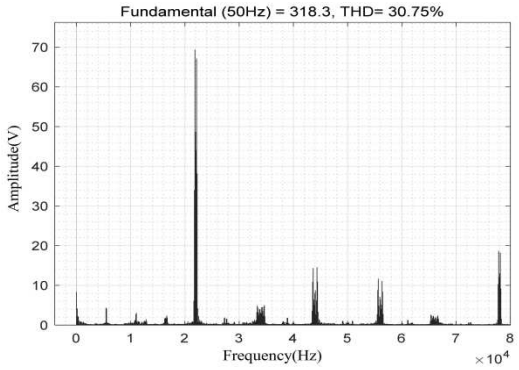
(c) Line voltage with 100% resistance and inductance load



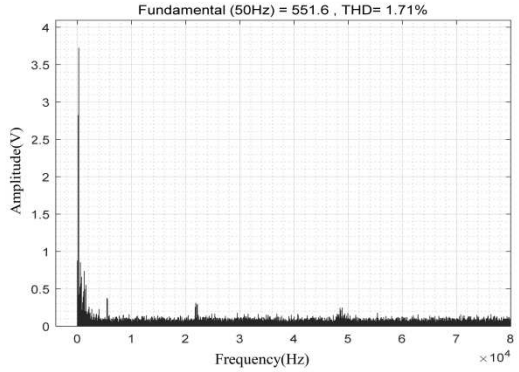
(d) Line voltage with 35% nonlinear load

FIGURE 11. Test waveforms of the proposed novel topology under various load modes

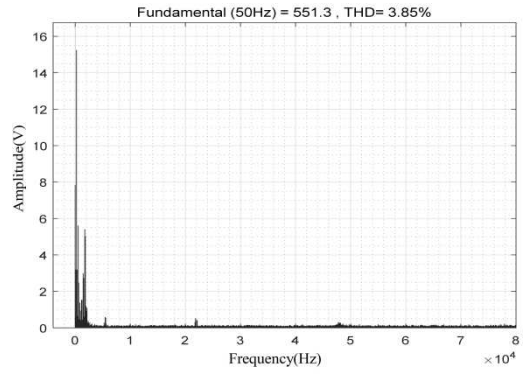
As shown in Figs. 13 and 14, the adoption of the CPS strategy cuts the CM voltage amplitude at the switching frequency down to one-sixth of that recorded in the absence of this strategy, which in turn enables a considerable decrease in the size and weight of the EMI filter.



(a) Voltage harmonic analysis of transformer secondary side phase voltage

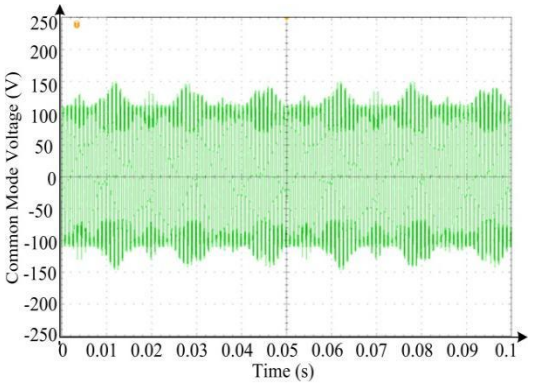


(b) Voltage harmonic analysis of 100% resistance-inductance load

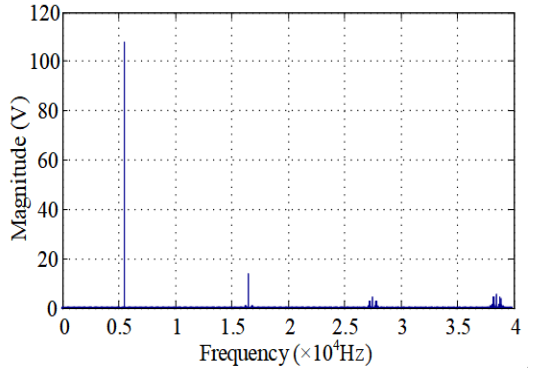


(c) Voltage harmonic analysis of 35% nonlinear load

FIGURE 12. Fourier spectrum analysis on experimental waveforms of the novel topology

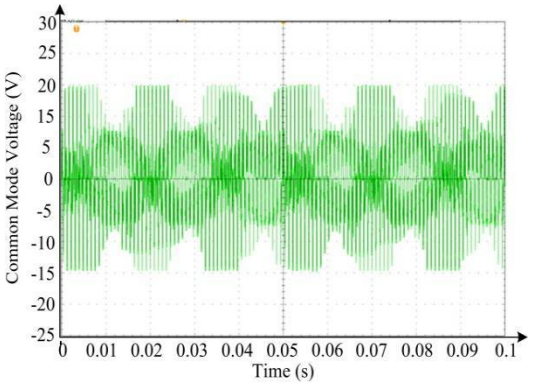


(a) Measured waveform of the output CM voltage

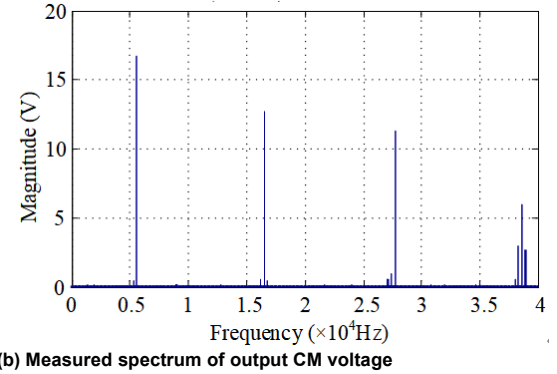


(b) Measured spectrum of output CM voltage

FIGURE 13. Measured results of output CM voltage in the absence of CPS modulation



(a) Measured waveform of output CM voltage



(b) Measured spectrum of output CM voltage

FIGURE 14. Measured results of output CM voltage with implemented CPS modulation

At 35% of the rated load, a comparison of the measured, simulated, and calculated primary-side current values of the 3D wound core transformer is presented in Fig. 15, with detailed numerical comparisons enumerated in Tab. 2.

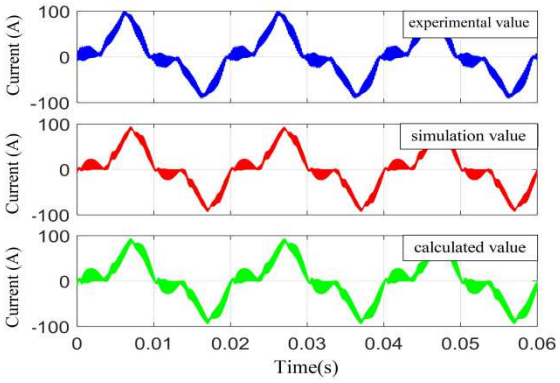


FIGURE 15. Comparison of primary side current test value, calculated value and simulation value under load steady state condition

TAB.2 COMPARATIVE ANALYSIS OF PRIMARY CURRENT HARMONIC SPECTRA UNDER STEADY-STATE LOAD OPERATION

Frequency (Hz)	50	150	13050	25850	26150
Experimental value (V)	58.430	23.870	2.783	4.914	4.726
Simulative value (V)	58.050	26.401	1.746	3.872	3.647
Relative error (%)	0.65%	10.60%	37.26%	21.20%	22.83%
Calculated value (V)	58.380	25.740	2.874	4.755	4.442
Relative error (%)	0.09%	7.83%	3.27%	3.24%	6.01%

It can be seen from Fig. 15 and Table 2 that the measured value of the fundamental component amplitude of the primary-side current matches well with the simulated and calculated results. At the same time, the main harmonic components located in the sidebands of the multiple switching frequency also show a high degree of coherence. These findings confirm the validity of the proposed transformer design, and further prove that the transformer's leakage inductance can be used as an effective substitute for the dedicated output filter inductor. The actual filtering performance aligns with theoretical design expectations, showing that the constructed theoretical and simulation models can provide practical guidance for the transformer's engineering design.

6 Conclusion

This study puts forward a novel three-phase dual-stage inverter topology, which boosts the equipment's power density through the integration of multiphase technology, CPS modulation, transformer magnetic integration design, and a 3D wound core configuration. The series connection of the transformer's secondary windings effectively elevates the utilization efficiency of DC voltage. In contrast to existing research findings, the fabricated prototype achieves performance metrics on par with those of cutting-edge high-frequency isolated topologies in terms of volume power density, weight power density, and energy efficiency, under the hybrid cooling system that combines closed-loop water cooling and auxiliary air cooling. This proposed topology is particularly well-suited for high-power scenarios that demand high efficiency, high reliability, high power density, and excellent cost-effectiveness.

Declarations

1. Acknowledgments： This research was funded by the Initial Scientific Research Foundation for Talented Scholars of Nanchang Institute of Science and Technology (Grant numbers NGRCZX-24-10), and Natural Science Foundation of Hubei Province : Research on early failure mechanism and defect detection technology of high power IGBT (Grant numbers 2022CFB488).

2. Author contributions： **Yong Tang**: Conceptualization, Methodology, Supervision, Project administration, Writing – review & editing. **Huiying Tang**: Formal analysis, Investigation, Data curation, Writing – original draft, Corresponding author, responsible for overall manuscript communication and revision. **Bo Wang**: Validation, Experimental design, Software, Visualization, contributed to prototype fabrication and experimental data collection.All authors have read and approved the final version of the manuscript and agree to the submission for publication.

3. Clinical trial number： This study focuses on the theoretical and experimental research of power electronic converter topology and its control strategy, which does not involve any clinical trials on human or animal subjects. No clinical trial number is applicable for this work.

4. Conflicts of interest： The authors declare that they have no known competing financial interests or personal relationships that could have appeared to influence the work reported in this paper. All authors confirm that there are no conflicts of interest, financial or otherwise, related to the research content, data collection, and manuscript writing of this study.

5. Data availability statements： All data generated or analysed during this study are included in this published article.

References

[1] Ma Weiming, “Electromechanical power conversion technologies in vessel integrated power system,” Journal of Electrical Engineering，vol.10, no.4, pp. 1-10, 2015.

[2] HADDADI A M, FARHANGI S, Blaabjerg F, “An isolated bidirectional single-stage inverter without electrolytic capacitor for energy storage systems,” IEEE Journal of Emerging and Selected Topics in Power Electronics, vol.7, no.3, pp. 2070-2080, 2019.

[3] RAHNAMAEE A, “Soft-switched hybrid-modulation for an isolated DC-link-capacitor-less pulsating-DC-link inverter,” Chicago: University of Illinois, pp.11-13, 2015.

[4] MCMURRAY W, “The thyristor electronic transformer: a power converter using a high-frequency link,” IEEE Transaction on Industry and General Applications, vol.7, no.4, pp. 451-457, 1971.
[5] ESPELAGE P M, BOSE B K, “High-frequency link power conversion,” IEEE Transactions on Industry Applications, vol.13, no.5, pp. 387-394, 1977.
[6] MENG Ming, WU Haibo, GUO Yu, “Analysis of high frequency transformer leakage in photovoltaic inverter,” Proceedings of 2011 International Conference on Mechatronic Science, Electric Engineering and Computer (MEC), pp. 1761-1764, Jilin, 2011.
[7] KEYHANI H, TOLIYAT H A, “Single-stage multistring PV inverter with an isolated high-frequency link and soft switching operation,” IEEE Transactions on Power Electronics, vol.29, no.8, pp. 3919-3929, 2014.
[8] LABELLA T, YU Wensong, LAI J, et al, “A bidirectional switch-based wide-input range high-efficiency isolated resonant converter for photovoltaic applications,” IEEE Transactions on Power Electronics, vol.29, no.7, pp. 3473-3484, 2014.
[9] ZHU Wenjie, ZHOU Keliang, CHENG Ming, “A bidirectional high-frequency-link single-phase inverter: modulation, modeling, and control,” IEEE Transactions on Power Electronics, vol.29, no.8, pp. 4049-4057, 2014.
[10] SONG Zhanfei, CHEN Wu, “Novel DC-AC inverter based on phase-shift shoot-through controlled dual-active-bridge and high-frequency pulse DC link,” IET Power Electronics, vol.12, no.14, pp. 3842-3851, 2019.
[11] PRASANNA U R, RATHORE A K, “Dual three-pulse-modulation (DTPM) based high-frequency pulsating DC link two-stage three-phase inverter for electric/hybrid/fuel cell vehicles applications,” IEEE Journal of Emerging and Selected Topics in Power Electronics, vol.2, no.3, pp. 477-486, 2014.
[12] MIN Byung-Duk, LEE Jong-Pil, KIM Jong-Hyun, et al, “A new topology with high efficiency throughout all load range for photovoltaic PCS,” IEEE Transactions on Industrial Electronics, vol.56, no.11, pp. 4427-4435, 2009.
[13] WANG Mengqi, GUO Suxuan, HUANG Qingyun, et al, “An isolated bidirectional single-stage DC-AC converter using wide-band-gap devices with a novel carrier-based unipolar modulation technique under synchronous rectification,” IEEE Transactions on Power Electronics, vol.32, no.3, pp. 1832-1843, 2017.
[14] IYER K V, BARANWAL R, MOHAN N, “A high-frequency AC-link single-stage asymmetrical multilevel converter for grid integration of renewable energy systems,” IEEE Transactions on Power Electronics, vol.32, no.7, pp. 5087-5108, 2017.
[15] KREIN P T, BALOG R S, GENG Xin, “High-frequency link inverter for fuel cells based on multiple-carrier PWM,” IEEE Transactions on Power Electronics, vol.19, no.5, pp. 1279- 1288, 2004.
[16] WANG Mengqi, HUANG Qingyun, GUO Suxuan, et al, “Soft switched modulation techniques for an isolated bidirectional DC-AC,” IEEE Transactions on Power Electronics, vol.33, no.1, pp. 137-150, 2018.
[17] DENG Songquan, MAO Hong, MAZUMDAR J, et al, “A new control scheme for high-frequency link inverter design,” Proceedings of 18th Annual IEEE Applied Power Electronics Conference and Exposition, pp. 512-517, Miami Beach, 2003.
[18] GANGAVARAPU S, VERMA M, RATHORE A K, “A novel transformerless single-stage grid-connected solar inverter,” IEEE Journal of Emerging and Selected Topics in Power Electronics, vol.11, no.1, pp. 970-980, 2023.
[19] Jiang Dong, Shen Zewei, Liu Zicheng, et al, “Progress in active mitigation technologies of power electronics noise for electrical propulsion system,” Proceedings of the CSEE, vol.40, no.16, pp. 5291-5301, 2020.
[20] Pindoriya R M，Mishra A K，Rajpurohit B S，et al, “An analysis of vibration and acoustic noise of BLDC motor drive,” 2018 IEEE Power & Energy Society General Meeting(PESGM)，Portland，2018.
[21] Huang Yingliang，Xu Yongxiang，Li Yong，et al, “PWM frequency voltage noise cancelation in three-phase VSI using the novel SVPWM strategy,” IEEE Transactions on Power Electronics，vol.33, no.10, pp. 8596-8606, 2018.
[22] Miyama Y，Ishizuka M，Kometani H，et al, “Vibration reduction by applying carrier phase-shift PWM on dual three-phase winding permanent magnet synchronous motor,” IEEE Transactions on Industry Applications，vol.54, no.6, pp. 5998-6004, 2018.
[23] Zhang Yichang， Ye Shangbin， Zhang Jiajia， et al, “Review of conducted noise suppression method for power electronic and electrical equipment,” Transactions of China Electrotechnical Society, vol.32, no.14, pp. 77-86, 2017.
[24] Chen Guocheng， Cao Dapeng， Zhang Yi， et al, “Harmonic characteristic analysis based on a three-phase tripled series-connected voltage source inverter,” Transactions of china electrotechnical society，vol.22, no.7, pp. 58-62, 2007.
[25] Yang Lü，Zhang Junhong，Wang Tiejun，et al, “A round shape phase-shift transformer applied in multi-module inverter,” Power electronics，vol.51, no.1, pp. 99-101, 2017.
[26] Dou Xiang，Xu Ningbo，Sun De, “Research on parallel phase shifted SPWM multiplex technology for H-bridge inverter circuit,” Foreign electronic measurement technology，vol.37, no.8, pp. 52-56, 2016.
[27] Zhao Jinghong，Ma Yuanzheng，Sun Pan, “Multi-module inverter system based on linear phase-shifting transformer,” Electric power automation equipment，vol.39, no.12, pp. 183-187, 2019.
[28] WooJun Cha，KyuTae Kim，YongWon Cho，et al, “Evaluation and analysis of transformerless photovoltaic inverter topology for efficiency improvement and reduction of leakage current,” IET Power Electron，vol.8, no.2, pp. 255-267, 2015.
[29] Wang Hengli，Fu Lijun，Jie Guisheng，et al, “Optimal control of three-phase inverter based on state-feedback with proportional resonant control,” Journal of XI’AN Jiaotong university, vol.47, no.8, pp. 127-132, 2013.
[30] Wang Hengli，Fu Lijun，Xiao Fei，et al, “A double-loop control strategy for three-phase inverter with unbalanced load,” Power system technology，vol.37, no.2, pp. 398-404, 2013.



Yong Tang was born in Xiangtan, Hunan Province in 1977. He graduated from Naval University of Engineering in electrical engineering with a doctor's degree in 2010. He is currently employed at School of Information and Artificial Intelligence, Nanchang Institute of Science and Technology, and his main research interests are in model, reliability and application of power electronic devices.



Huiying Tang was born in Nanyang, Henan Province in 1985. She graduated from Wuhan Institute of Technology in electrical engineering with a master's degree in 2013. She is currently employed at Wuhan Donghu University, and her main research interests are in electrical devices and power electronics technology.



Bo Wang was born in Wuhan, Hubei Province in 1980. He graduated from Naval University of Engineering in electrical engineering with a doctor's degree in 2012. He is currently employed at School of Information and Artificial Intelligence, Nanchang Institute of Science and Technology, and his main research interests are in electrical devices and power electronics technology.